DISTORTION COMPENSATION FOR GENERALIZED STEREOSCOPIC PARTICLE IMAGE VELOCIMETRY

Steven M. Soloff, **Ronald J. Adrian**, and **Zi-Chao Liu**
Department of Theoretical and Applied Mechanics
University of Illinois at Urbana-Champaign
Urbana, Illinois, USA 61801

Abstract

Optical distortion caused by inaccurate optical alignment, lens nonlinearity, and/or refraction by optical windows, fluid interfaces, and other optical elements of an experiment cause inaccuracy by introducing variable magnification. Since fractional changes in the magnification have a one-to-one effect on the accuracy of measuring the velocity, it is important to compensate for such distortions. A general experimental calibration procedure is described which determines the magnification matrix of a distorted imaging system, and an algorithm is presented to compute accurate velocity field displacements from measurements of distorted PIV images. These procedures form a basis for generalized stereoscopic PIV procedures which permit easy electronic registration of multiple cameras and accurate recombination of stereoscopic displacement fields to obtain the three-dimensional velocity vector field.

1. Introduction

The accuracy of velocity measurement by particle image velocimetry (PIV) or particle tracking velocimetry (PTV) depends upon the accuracy with which image displacements can be measured and the accuracy with which image displacements can be related to particle locations and their respective particle displacements. (A third factor, the accuracy with which particle displacements are equal to fluid displacements, is not considered here.) These factors depend in turn on two types of optical aberrations: focusing aberrations which cause the particle images to be enlarged, making it more difficult to measure displacements accurately, and image distortion which creates a nonlinear relationship between the location of a particle and the location of its image. Focusing aberrations include spherical aberration, astigmatism, and coma (Jenkins and White 1957). Image distortion refers to any agency that causes the magnification to vary as a function of position in the field of the image.

There are three agencies that cause the magnification in an experiment to vary. The first is design imperfection in the lens. The second is refraction caused by anything, including windows and fluid interfaces, that lies between the object plane in the illuminating light sheet and the image plane (c.f. Prasad and Adrian 1993, for example). The third is misalignment of the image recording plane with respect to the object plane. The image recording plane is the surface of the film or the video array on which the image is actually recorded, and it need not coincide with the image plane in which all images are in ideal focus. Even if they do coincide, the magnification is not constant unless the image plane is parallel to the object plane, as in lateral-offset stereoscopic cameras, such as those described in Arroyo and Greated (1991) and Grant *et al.* (1995). This last distortion necessarily occurs in angular-offset stereoscopic cameras in which the image plane is rotated with respect to the object plane in order to bring the images into better focus (Prasad and Jensen 1995). It also occurs in single lens cameras and in lateral-offset stereoscopic cameras due to imperfect alignment of the recording plane with the object plane.

The PIV recording and interrogation processes are illustrated in Fig. 1 for the case of zero distortion. The image of any particle is simply located by the chief ray that extends from the particle through the center of the lens to the image plane. Choosing coordinate systems in the object and image planes with origins **Ox** and **OX** on the optic axis of the lens, the following simple relationship results:

$$(X,Y)=-M(x,y)\,, \qquad (1)$$

where $\mathbf{X} = (X, Y)$ is the image location and (x, y) is the object location formed from the projection of $\mathbf{x} = (x, y, z)$ onto the xy-plane. The magnification is

$$M=\frac{d_i}{d_o-z}\,, \qquad (2)$$

in which d_i is the image distance and d_o is the object distance.

The case of nonzero distortion is illustrated in Fig. 2. Here, a curved window acts like a weak lens to refract the chief ray, and the image recording plane is tilted with respect to the object plane. Both of these effects cause some blurring of the point response image on the recording plane, but as noted above, that blurring may be small enough to permit successful

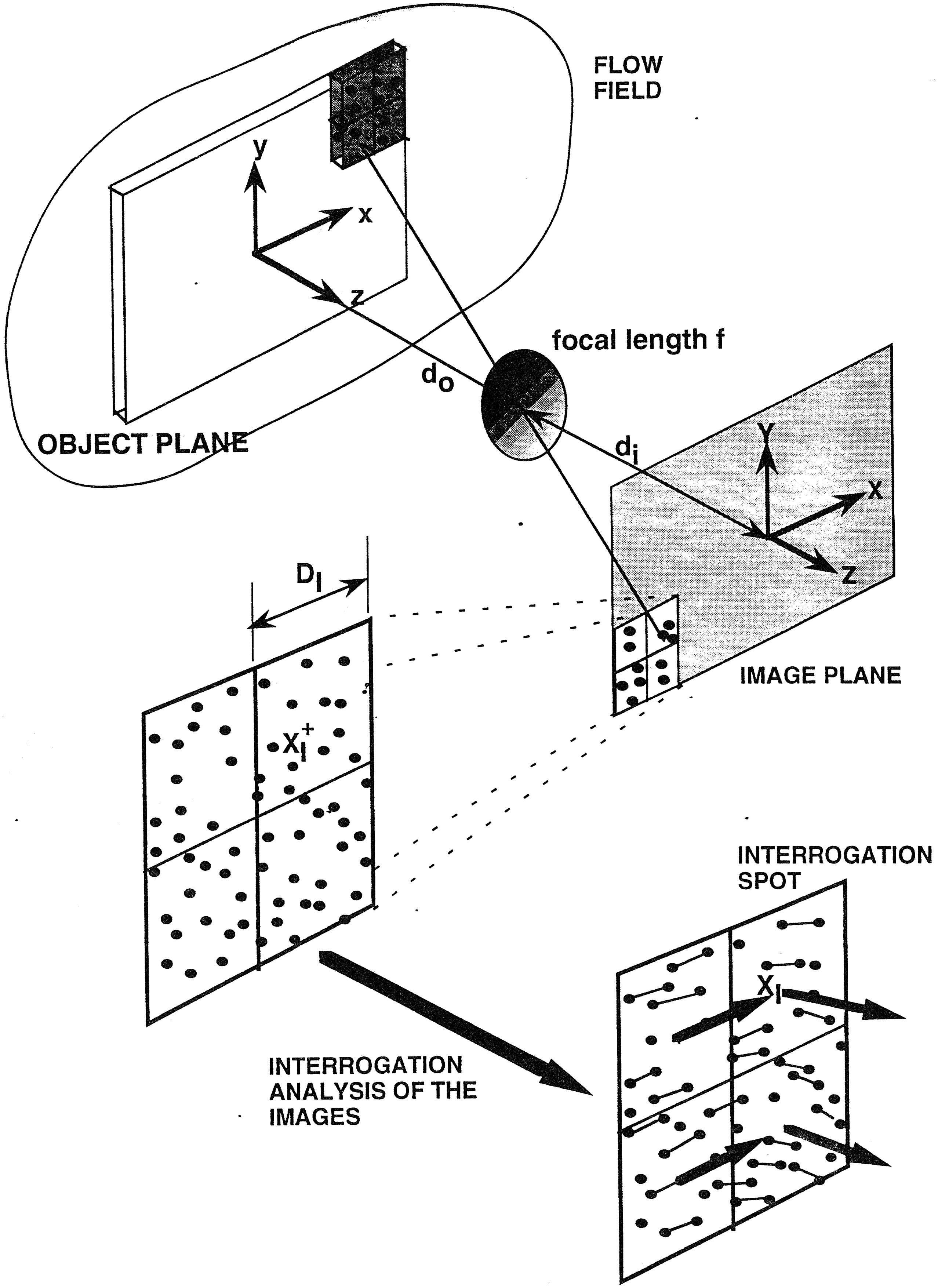

Figure 1. PIV recording and interrogation processes for a single camera with zero distortion. $\mathbf{X}_I$ is the location of the center of the interrogation spot on the image plane.

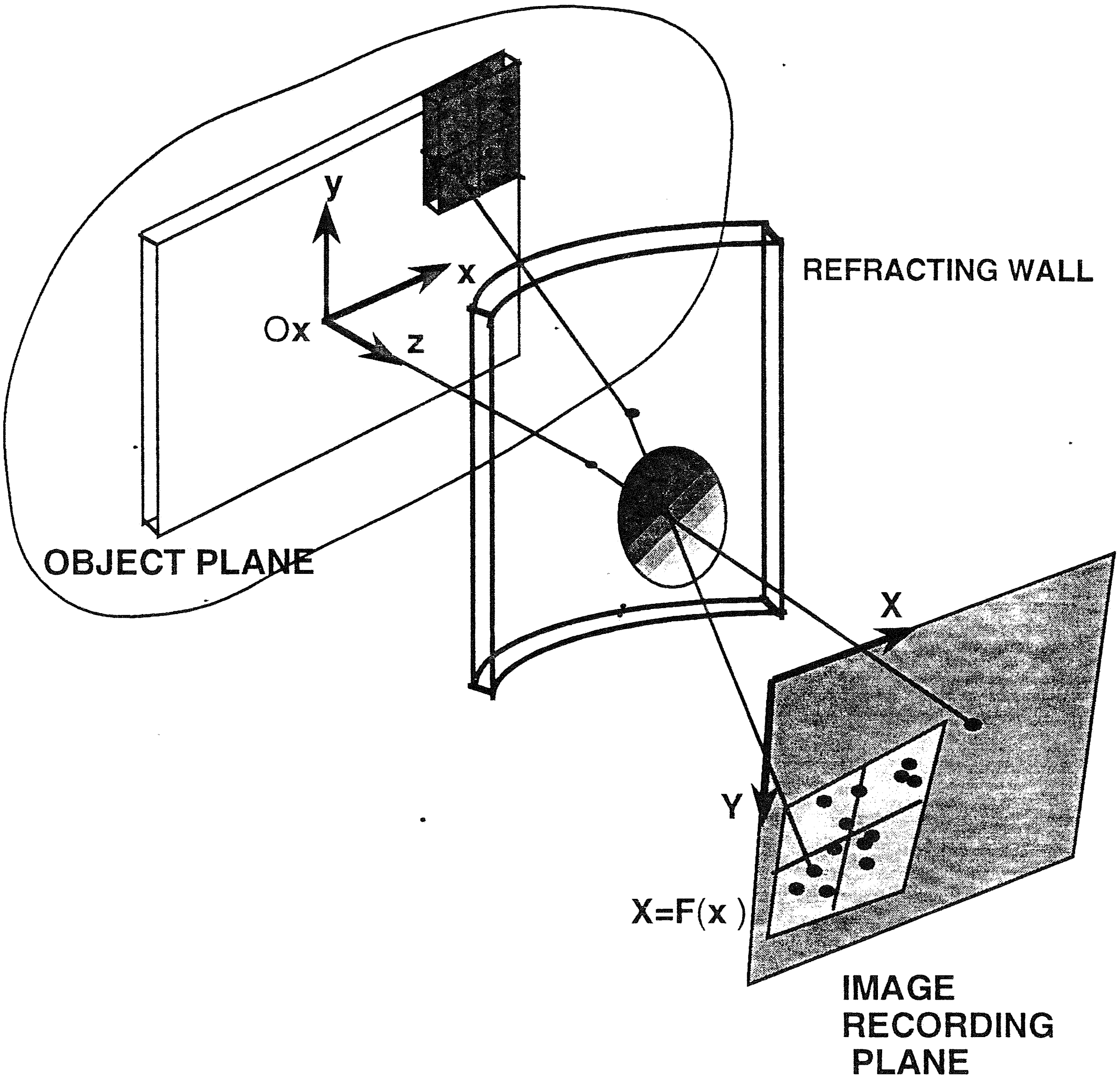

Figure 2. PIV recording process for a single camera with nonzero distortion. **F**(**x**) is the mapping function for the camera that relates positions in the object plane to positions in the image plane.

measurement of the image displacements despite significant distortion. The reference frame **X** is embedded in the recording frame, i.e. $Z = 0$, and since it is normally associated with the pixel index array, its orientation in this general case with respect to the object plane is allowed to be arbitrary. In general the relationship between positions in the three-dimensional physical space of the flow, **x**, and the positions in the two-dimensional image recording plane, **X**, can be described by a nonlinear mapping function,

$$\mathbf{X}=\mathbf{F}(\mathbf{x}), \tag{3}$$

that replaces the simple linear relationship in Eq. (1). Note that **x** in this equation is the full, three-dimensional vector.

Variable magnification introduces systematic bias errors into the measurement of fluid velocity and the location of the velocity vector. Being systematic, the distortion bias can be corrected by an appropriate technique based either on a mathematical model of the distortion, as in Prasad and Adrian (1993), or on an experimental calibration, as in the calibration for particle tracking velocimetry described by Kent *et al.* (1993). In the work presented here, a calibration is used to generate an approximate mapping function. Distortion can be compensated even when the focusing aberrations cause some blurring of the images, so long as the blurring is not so severe as to make the measurement of image locations impossible or unacceptably inaccurate.

The information found by calibration can be used to do more than correct for distortion. Most PIV interrogation analyses determine the velocity vectors on a uniform grid fixed in the pixel array of the video camera, and the user has no ability to request data on a non-uniform grid *in the fluid* that may be more appropriate for the flow under consideration. A side benefit of using the mapping function algorithm described here is that the measured vectors can be interpolated onto any grid within the domain of the mapping function.

The use of a general mapping function found by calibration is very helpful in the physical construction of a stereoscopic PIV camera because it eliminates the need to mechanically register the pixel arrays of multiple cameras, replacing this process by a simple mathematical registration. In addition, it will be shown how the mathematics of the mapping function provides a natural framework in which to combine the images of two or more cameras to obtain the three-dimensional vector field.

2. Displacement Equations

2.1 Single Camera

Consider first the displacement of one particle as recorded by a single camera. Following this analysis the results will be generalized to the displacement of groups of particles, as measured by PIV correlation techniques. In the next section, the results will be applied to stereoscopic cameras.

Between exposures at times t and $t + \Delta t$ a particle at **x** moves to $\mathbf{x} + \Delta\mathbf{x}$. The displacement of its image is

$$\Delta\mathbf{X}=\mathbf{F}(\mathbf{x}+\Delta\mathbf{x})-\mathbf{F}(\mathbf{x}). \tag{4}$$

To first order the displacement is approximated by

$$\Delta \mathbf{X} \cong \nabla \mathbf{F}(\mathbf{x}) \Delta \mathbf{x}, \tag{5}$$

where the gradient,

$$(\nabla \mathbf{F})_{ij} = \frac{\partial F_i}{\partial x_j} = F_{i,j}, \quad i = 1,2 \text{ and } j = 1,2,3, \tag{6}$$

is clearly a generalization of the usual concept of magnification. We shall call it the *magnification matrix.* As an example, and for later reference, the magnification matrix for perfectly linear imaging is, from Eq. (1),

$$F_{i,j}(\mathbf{x}) = \frac{-d_i}{d_o - z} \begin{pmatrix} 1 & 0 & \dfrac{x}{d_o - z} \\ 0 & 1 & \dfrac{y}{d_o - z} \end{pmatrix}. \tag{7}$$

The terms in the last column, $F_{1,3}$ and $F_{2,3}$, represent the effect of perspective.

In PTV the displacement of the image of an individual particle, $\Delta\mathbf{X}$, is determined by image analysis, and one must then relate that displacement to displacement in the physical space, $\Delta\mathbf{x}$. Eq. (4), or more commonly the approximate Eq. (5), can provide the necessary relationship when distortions are present, but there are two problems in executing the last step. First, since $\mathbf{X}$ is two-dimensional and $\mathbf{x}$ is three-dimensional, there is not a unique relationship between $\mathbf{X}$ and $\mathbf{x}$. The particle could lie anywhere along the chief ray that extends from the image point through the center of the lens. Second, since $F_{i,j}$ is a 2×3 matrix, there is no unique inverse solution of (4) or (5) for $\Delta\mathbf{x}$ in terms of $\Delta\mathbf{X}$. These difficulties exist whether the imaging is distorted or not, and they are simply a consequence of the effect of perspective (Adrian 1991). In deep-field PTV (i.e. photogrammetry), the solution is to use two (or possibly more) cameras, each giving measurements of image locations in two directions (Nishino *et al.* 1989, Maas *et al.* 1993, and Guezennec *et al.* 1994). Then, the number of measured image displacements exceeds the number of unknowns and both $\mathbf{x}$ and $\Delta\mathbf{x}$ can be found.

In light sheet PIV, the situation is a little different because the thickness of the light sheet, Δz_o, is normally very small compared to the object distance, d_o, and the width of the field of view in the fluid, l, may, in certain cases, also be small compared to d_o. These conditions allow certain approximations to be made. Specifically, consider a PIV measurement of displacement that is made in an interrogation spot centered at $\mathbf{X}_I$ on the image plane. It is known (Adrian 1988) that a PIV measurement by correlation yields, on average, a measurement of the velocity field of the fluid averaged over a volume consisting of the intersection of the interrogation spot, projected back into the fluid with the thickness of the light sheet, Δz_o (c.f. Fig. 1). This volume is called the *interrogation cell.* The center of the interrogation spot $\mathbf{X}_I$ maps back into a point that intersects the mid-plane of the light sheet at

$$\mathbf{x}_I = (x_I, y_I, 0), \tag{8}$$

where

$$\mathbf{X}_I = \mathbf{F}(\mathbf{x}_I). \tag{9}$$

This is the center of the interrogation cell, and since $\mathbf{x}_I$ is two-dimensional ($z_I = 0$) it is possible to associate each $\mathbf{X}_I$ with a unique $\mathbf{x}_I$, thereby resolving the first difficulty cited above.

The first-order relationship between an image plane displacement, $\Delta\mathbf{X}(\mathbf{X}_I)$, and object plane displacement, $\Delta\mathbf{x}(\mathbf{x}_I)$, is derived by Taylor series expansion of Eq. (4) about the point $\mathbf{x}_I$, followed by volume averaging the equation over the interrogation cell, with suitable transformations between $\mathbf{x}$ and $\mathbf{X}$. Denoting averages over the interrogation cells in $\mathbf{x}$ and $\mathbf{X}$ by overbars, and neglecting any variation of the magnification matrix over the dimensions of the interrogation cell (justified when the dimensions of the interrogation cell are much smaller than the object distance), one finds the following set of equations:

$$\overline{\Delta X_i} \cong F_{i,j}(\mathbf{x}_I)\overline{\Delta x_j}, \quad i = 1,2 \text{ and } j = 1,2,3, \tag{10a}$$

or

$$\begin{pmatrix} \overline{\Delta X_1} \\ \overline{\Delta X_2} \end{pmatrix} = \begin{pmatrix} F_{1,1} & F_{1,2} & F_{1,3} \\ F_{2,1} & F_{2,2} & F_{2,3} \end{pmatrix} \begin{pmatrix} \overline{\Delta x_1} \\ \overline{\Delta x_2} \\ \overline{\Delta x_3} \end{pmatrix}. \tag{10b}$$

This is the final operative system of equations for interpreting PIV measurements in the presence of distortion. If the distortion is severely nonlinear, or if very high accuracy is needed in the relationship between $\overline{\Delta\mathbf{X}}$ and $\overline{\Delta\mathbf{x}}$, and justified by the accuracy of the measurements of $\overline{\Delta\mathbf{X}}$, this relationship can be improved by retaining higher order terms in the Taylor series expansion. The work presented here assumes that a linear expansion is adequate, as is standard practice in all PIV work done to date.

For the case of a single camera, the system of equations in (10) cannot be solved for $\Delta\mathbf{x}(\mathbf{x}_I)$ as it stands because there are still only two equations for three unknowns. Common practice in PIV with one camera is to ignore the effect of perspective, as embodied in the terms $F_{1,3}$ and $F_{2,3}$, thereby reducing Eq. (10b) to

$$\begin{pmatrix} \overline{\Delta X_1} \\ \overline{\Delta X_2} \end{pmatrix} = \begin{pmatrix} F_{1,1} & F_{1,2} \\ F_{2,1} & F_{2,2} \end{pmatrix} \begin{pmatrix} \overline{\Delta x_1} \\ \overline{\Delta x_2} \end{pmatrix}. \tag{11}$$

This is justified if $F_{1,3}$ and $F_{2,3}$ are small. Some guidance concerning the magnitude of the perspective effect can be gained by considering the expression for the magnification matrix at $\mathbf{x}_I$ for perfectly linear imaging:

$$F_{i,j}(\mathbf{x}_I) = \frac{-d_i}{d_o} \begin{pmatrix} 1 & 0 & \dfrac{x_I}{d_o} \\ 0 & 1 & \dfrac{y_I}{d_o} \end{pmatrix}. \tag{12}$$

It is clear that the perspective effect is small if x_I and y_I are both small compared to d_o for all values of x_I and y_I, i.e. over the full field-of-view. This condition is referred to as *paraxial imaging* (Adrian 1991). It is expected that paraxial imaging will lead to small magnitude of the perspective effect in the case of distorted imaging, as well, but this must be verified in individual cases.

Unfortunately, it is quite common for the paraxial condition to be only weakly satisfied. For example, consider a typical laboratory configuration in which a 100 mm wide field-of-view is imaged at an object distance of 500 mm. The position x_I varies from –50 mm to +50 mm, implying that $F_{1,3}$ varies between –0.1 and +0.1. Thus, without correcting for perspective, measurements of the in-plane velocity components are contaminated by as much as 10% of the out-of-plane velocity. If the flow is two-dimensional in the xy-plane, i.e. $w = 0$, there is no error, but if the out-of-plane component is comparable to the in-plane component, errors of order 10% are incurred. Stereoscopic imaging provides the only unconditional solution to the problem of compensating for perspective, and it will be considered in the next section.

2.2 Stereoscopic Camera

For a stereoscopic system, two cameras are involved in deriving the displacement equations, which requires a slight change in notation. The displacement of a particle image on camera c, where $c = 1, 2$, is

$$\Delta\mathbf{X}^{(c)} = \mathbf{F}^{(c)}(\mathbf{x}+\Delta\mathbf{x}) - \mathbf{F}^{(c)}(\mathbf{x})\,. \tag{13}$$

Performing a Taylor series expansion of Eq. (13) and volume averaging over the interrogation cell, similarly to what was done in the previous section, one finds the first-order relationship between an image plane displacement on camera c, $\Delta\mathbf{X}^{(c)}(\mathbf{X}_I)$, and an object plane displacement, $\Delta\mathbf{x}(\mathbf{x}_I)$, to be

$$\overline{\Delta X_i^{(c)}} \cong F_{i,j}^{(c)}(\mathbf{x}_I)\overline{\Delta x_j}, \quad i = 1,2 \text{ and } j = 1,2,3\,. \tag{14}$$

Eq. (14) provides a system of equations for each camera. Writing out both sets of equations in full and augmenting them yields

$$\begin{pmatrix} \overline{\Delta X_1^{(1)}} \\ \overline{\Delta X_2^{(1)}} \\ \overline{\Delta X_1^{(2)}} \\ \overline{\Delta X_2^{(2)}} \end{pmatrix} = \begin{pmatrix} F_{1,1}^{(1)} & F_{1,2}^{(1)} & F_{1,3}^{(1)} \\ F_{2,1}^{(1)} & F_{2,2}^{(1)} & F_{2,3}^{(1)} \\ F_{1,1}^{(2)} & F_{1,2}^{(2)} & F_{1,3}^{(2)} \\ F_{2,1}^{(2)} & F_{2,2}^{(2)} & F_{2,3}^{(2)} \end{pmatrix} \begin{pmatrix} \overline{\Delta x_1} \\ \overline{\Delta x_2} \\ \overline{\Delta x_3} \end{pmatrix}, \tag{15a}$$

or

$$\overline{\Delta\mathbf{X}_A} = (\nabla\mathbf{F})_A\overline{\Delta\mathbf{x}}\,, \tag{15b}$$

where the subscript A denotes the appropriate augmented entity. This is the final operative system of equations for a stereoscopic camera for interpreting PIV measurements in the presence of distortion.

Although it appears that the system in (15) is overdetermined, this is not necessarily the case. If no errors are incurred when measuring the image displacements, two of the equations will be dependent simply due to the nature of the optics. For example, if a purely x_3-displacement is observed by a stereocamera, the perceived x_2-displacement on both cameras will be identical, but the perceived x_1-displacement will be in opposite directions on each camera. Thus, the second and fourth equations in (15) will be linearly dependent. Several approaches could then be used to solve the system. For example, the two dependent equations could be added together yielding a solvable system. However, random errors are incurred when measuring the image displacements, so it may not be the case that two of the equations will be exactly dependent. For the general case where the redundancy is not obvious, a least-squares solution should be used to minimize the squared Euclidean norm of the residual,

$$\varepsilon = \left| \overline{\Delta \mathbf{X}_A} - (\nabla \mathbf{F})_A \overline{\Delta \mathbf{x}} \right|^2 . \tag{16}$$

3. Procedure for Single Camera

The purpose of the calibration is to determine how positions in the object plane map to positions in the image plane taking into account all aberrations. In order to do this it is necessary to acquire images of a *calibration target* whose location in the object plane is known. Design of the calibration target is the most important part of performing a successful calibration. In general, different experiments may require different calibration targets.

The target must have some sort of characteristic marks on its face. These marks and their corresponding images will define how positions in the object plane map to positions in the image plane. The marks are placed on a precise, evenly spaced Cartesian grid. The size and shape of the target is constrained by the measurement container, but it must be large enough so that the characteristic marks occupy the entire field of view of the camera. In order to maximize the accuracy of the mapping function the field of marks should extend to the edges of the viewable field.

In general, the grid on the calibration target has two parameters: (1) the total number of points, and (2) the spacing between points (the size of a grid cell). These parameters should be chosen according to the size of the image acquisition area and the amount of distortion in the experiment. Thus, the number of grid points is proportional to the size of the image acquisition area, while the size of a grid cell is inversely proportional to the amount of distortion in the experiment.

A sometimes attractive alternative to a calibration grid is a single target point that can be moved precisely to many different locations. For example, Kent *et al.* (1993) describe a target on the end of an arm under control of a stepper motor. This approach is very useful for measuring the mapping function over a deep volume, as in photogrammetric PTV.

Ideally, one would like to find a mapping function **F** such that given any point **x** in the object plane, its corresponding location **X** in the image plane could be determined with complete accuracy. In reality, one cannot experimentally determine an **F** that will yield zero error for an arbitrarily complex geometry. Thus, an estimate for the mapping function, $\hat{\mathbf{F}}$, that has an analytic representation will be sought instead. Many possibilities arise at this point, but because of its simplicity, a multi-dimensional polynomial is an obvious choice. There are several ways to determine the polynomial. For example, one could use the method of least-squares to determine an $\hat{\mathbf{F}}$ that approximates the data while minimizing the mean square error,

$$\varepsilon = \frac{1}{N_c} \sum_{\{\mathbf{x}_c\}} \left| \mathbf{F}(\mathbf{x}_c) - \hat{\mathbf{F}}(\mathbf{x}_c) \right|^2 , \tag{17}$$

where the set $\{\mathbf{x}_c\}$ represents the collection of points on the calibration target, and N_c is the total number of points in the set. Alternatively, an interpolating spline could be used to determine local polynomials.

In all respects, the least-squares polynomial is the easiest form to implement and yields very good results unless the distortion is extremely severe. In these instances, a spline would be a better choice. A least-squares polynomial with cubic dependence in x_1 and x_2, but quadratic dependence in x_3, will be adopted as the mapping function estimate for the remainder of this paper. That is,

$$\begin{aligned}\hat{\mathbf{F}}(\mathbf{x}) = {} & \mathbf{a}_0 + \mathbf{a}_1 x_1 + \mathbf{a}_2 x_2 + \mathbf{a}_3 x_3 + \mathbf{a}_4 x_1^2 + \mathbf{a}_5 x_1 x_2 + \mathbf{a}_6 x_2^2 + \mathbf{a}_7 x_1 x_3 + \\ & \mathbf{a}_8 x_2 x_3 + \mathbf{a}_9 x_3^2 + \mathbf{a}_{10} x_1^3 + \mathbf{a}_{11} x_1^2 x_2 + \mathbf{a}_{12} x_1 x_2^2 + \mathbf{a}_{13} x_2^3 + \\ & \mathbf{a}_{14} x_1^2 x_3 + \mathbf{a}_{15} x_1 x_2 x_3 + \mathbf{a}_{16} x_2^2 x_3 + \mathbf{a}_{17} x_1 x_3^2 + \mathbf{a}_{18} x_2 x_3^2,\end{aligned} \qquad , \qquad (18)$$

where the $\mathbf{a}_i$ are vector-valued coefficients to be determined. It is noted, however, that the generalization to other methods of interpolation or approximation is trivial and should be done if it is warranted by the severity of the distortion.

Choosing $\hat{\mathbf{F}}$ to be a cubic function of x_1 and x_2 was a decision based purely on qualitative information. By viewing a Cartesian grid through various types of distorting media that might be found in a PIV or PTV experiment, it was observed that the curvature of the grid lines did not vary much. Thus, it was judged that a cubic polynomial could track the distortion produced in the most common cases reasonably well. The justification for selecting quadratic dependence in x_3 is due solely to the mathematical limitation that results from performing the calibration on only three x_3-planes. Generalizing the procedure to four or more planes would clearly allow higher-order terms in x_3, but for present purposes, three planes are adequate.

Before beginning the calibration procedure, one must define a coordinate system in the object plane and the image plane. The most common way to define the object-plane coordinate system is by specifying one of the characteristic marks on the face of the calibration target as the origin. The locations of all other characteristic marks are measured relative to this point. Normally, the origin of the image plane is defined by pixel (0,0) on a CCD array or the lower-left corner of a photograph. One must also make sure the experimental setup is in the exact configuration it will be in when measurements are taken.

The first step in the calibration procedure is to acquire a calibration image. This is simply an image of the calibration target as viewed by the camera in the current experimental setup. Before acquiring the image, the face of the calibration target should be aligned as precisely as possible with the center of the light sheet. Once aligned, the calibration image is acquired and stored.

The next step is to determine the locations of the characteristic marks on the calibration image with respect to the origin of the image plane. An accurate way to locate the marks is through a template-matching technique. This process is performed in a manner similar to the correlation procedure used in PIV. A template image is created that is similar to the shape of the characteristic marks on the calibration target. The template and calibration image are then correlated using two-frame cross-correlation, which is followed by a peak-searching routine to determine the pixel locations of the marks in the correlation plane. Sub-pixel accuracy can be attained by fitting a curve, such as a Gaussian or a quadratic polynomial, to the peak. Alternatively, for marks of an appropriate shape (e.g. circular), one can use a local centroid calculation, rather than template matching, to determine the locations of the marks. Once the locations of the target points in the image and object planes have been obtained, the coefficients of the mapping function in Eq. (18) can be determined using a least-squares procedure. Note that for a single camera the calibration image is acquired at only a single x_3 location (presumably at $x_3 = 0$). In this case, all terms in Eq. (18) involving x_3 are zero, and the corresponding coefficients are not determined by the calibration. This is acceptable because, as noted above, the single camera equations must ignore out-of-plane motion anyway.

Now that the system has been calibrated, one may proceed normally and acquire images using the conventional PIV technique. Once recorded, each image is then interrogated on a set of points $\{\mathbf{X}_I\}$ in the image plane that is determined by the interrogation software. The image plane displacements are then validated and filtered using appropriate software tools. Note that many interrogation software systems provide the user with very limited control over the grid. Commonly, one can manipulate only a few parameters, such as the location of the grid in the image plane and the number of interrogation points to use, and specifying an arbitrary grid for interrogation is not usually possible. Even if it were, locations in the image plane are not necessarily meaningful. One would prefer to be able to request particle displacements at locations in the object plane for which the coordinates of physically meaningful locations are known.

Because it is known how positions in the object plane map to positions in the image plane from the mapping function generated during the calibration procedure, it is possible to calculate particle displacements at any location in the fluid within the domain of the mapping function. The collection of points in the object plane where displacements are desired is denoted by $\{\mathbf{x}_g\}$ and their corresponding images by $\{\mathbf{X}_g\}$. The image displacements previously determined on $\{\mathbf{X}_I\}$ during the interrogation stage are interpolated onto $\{\mathbf{X}_g\}$ using an appropriate method, such as bilinear interpolation. Note that two potential problems can arise during this procedure. First, the image of a particular $\mathbf{x}_g$ may lie outside the image recording domain of the camera, i.e. the CCD chip or the film frame. Second, when interpolating image displacements onto a particular $\mathbf{X}_g$, one or more of its neighboring grid points may not contain data. In both cases, the $\mathbf{x}_g$ in question is discarded. At this point Eq. (11) is solved for the particle displacements in the fluid.

Fig. 3 is a flow chart that illustrates the processes described above to compute the particle displacements in the fluid. Process A represents the steps taken during the PIV experiment and ensuing interrogation process. Each step in Process A can be made within any of several different standard PIV processing software packages, including commercial software. Process B represents the procedure by which image displacements computed during process A are interpolated onto the mapping of the user-defined grid. Process C represents the calibration procedure. The results of processes B and C serve as input to Eq. (11), from which the particle displacements on the user-defined grid are calculated. Note that defining the grid $\{\mathbf{x}_g\}$ in the object plane and mapping it onto the image plane circumvents the nonlinear inverse problem of solving for object points in terms of image location.

4. Procedure for Stereoscopic Camera

The calibration procedure for a stereoscopic camera is very similar to that for a single camera (c.f. Fig. 4). However, because it is necessary to know how the magnification in the x_3-direction varies, one must acquire multiple calibration images at planes normal to the light sheet. Since a polynomial is being used to estimate the mapping function, the number of images acquired at different x_3 locations places an upper limit on the order of the x_3 terms. Keep in mind that a least-squares method is being used so that one could use more calibration images than the

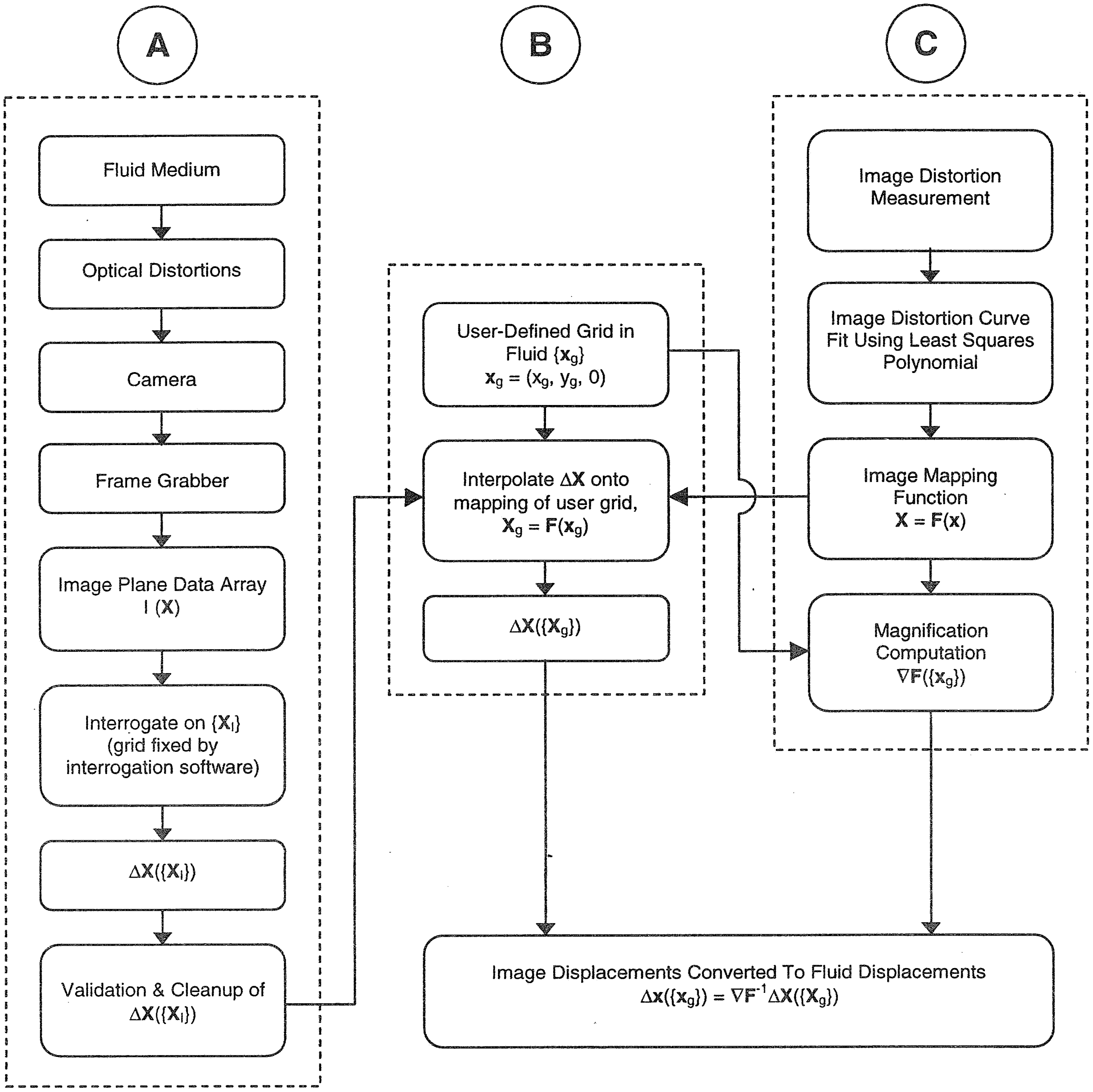

Figure 3. Flow chart for a single camera. Process A represents the standard PIV acquisition and interrogation procedure. Process B represents the procedure for computing displacements in the image plane corresponding to user-defined locations in the fluid. Process C represents the calibration procedure. The results of processes B and C are used to compute the particle displacements at user-defined locations in the fluid.

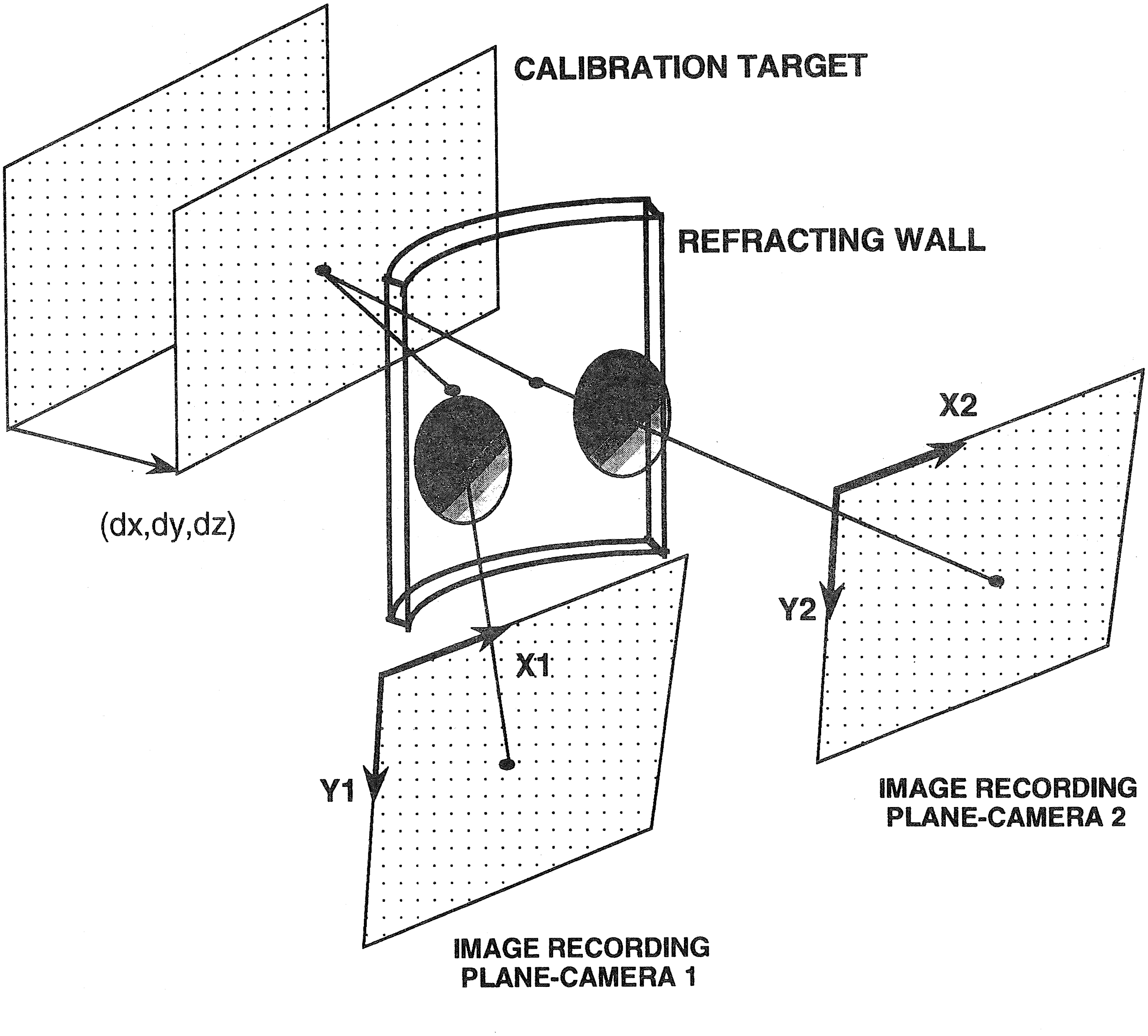

Figure 4. Schematic of the calibration procedure for a stereoscopic camera. The mapping function for each camera is valid over the volume of size dx × dy × dz traced out by the calibration target during the calibration procedure.

desired order of the x_3-terms in order to reduce the mean square error of the estimate. At a minimum, the second order polynomial in x_3 requires calibration data at three x_3-locations separated by a distance comparable to the thickness of the light sheet.

Once the calibration images for all planes have been acquired for each camera, the locations of the characteristic marks in each image are determined with respect to the origin of the corresponding image plane. The same procedure described in the previous section for locating the images of the calibration marks is applied to each image. Enough information is now available to determine the coefficients in Eq. (18) twice — once for each camera. As shown in §2.2, the resulting two mapping functions are all that is necessary to recombine a pair of 2-D velocity fields into a single planar 3-D velocity field.

Once the system has been calibrated, one can proceed normally and acquire images using the conventional PIV technique. The images for each camera are interrogated on a set of points $\{\mathbf{X}_I^{(c)}\}$ in the corresponding image plane that is determined by the interrogation software. The limitations mentioned in the previous section concerning user-control of the grid apply here, as well. The ability to specify a user-defined grid in the fluid, as in the single camera case, is applicable to the stereoscopic camera, also. The two problems that may arise during the interpolation of image displacements onto $\{\mathbf{X}_g^{(c)}\}$ can now occur for each camera individually. If a particular $\mathbf{x}_g$ has been deleted because of a problem that occurred during interpolation on either camera, stereo recombination cannot be performed at this location and a hole will appear in the final 3-D velocity field.

Fig. 5 is a flow chart that illustrates the processes described above to compute 3-D particle displacements in the fluid. The processes outlined in Fig. 3 are performed for each camera. The results of processes B1, B2, C1, and C2 are used to form the augmented system in Eq. (15), and the 3-D particle displacements on the user-defined grid are calculated. It should be noted that unlike the stereoscopic PIV recombination algorithm given in Prasad and Adrian (1993) in which the image plane interrogation grid and corresponding image displacements were inversely mapped into the fluid followed by the determination of a common Cartesian grid to interpolate displacements onto, the algorithm presented here requires no such procedure. The entire process is simplified by mapping the user-defined grid $\{\mathbf{x}_g\}$ onto each image plane and performing the interpolation of displacements therein.

5. Application and Evaluation of Calibration Procedure

In this section, we present the results of applying the calibration procedure to both a single camera and a stereoscopic camera. In each case, a computer-generated image was displaced by a known amount in the object plane and the corresponding image displacements were computed using TSI INSIGHT PIV software. Mapping functions were used to compute the fluid displacement from this information and errors are plotted. Unless otherwise mentioned, the uncertainty in any experimental displacements of the image is ± 5 μm.

5.1 Single Camera

The setup for the single camera experiment is shown schematically in Fig. 6. In order to test the robustness of the calibration procedure, a distorting medium was purposely placed

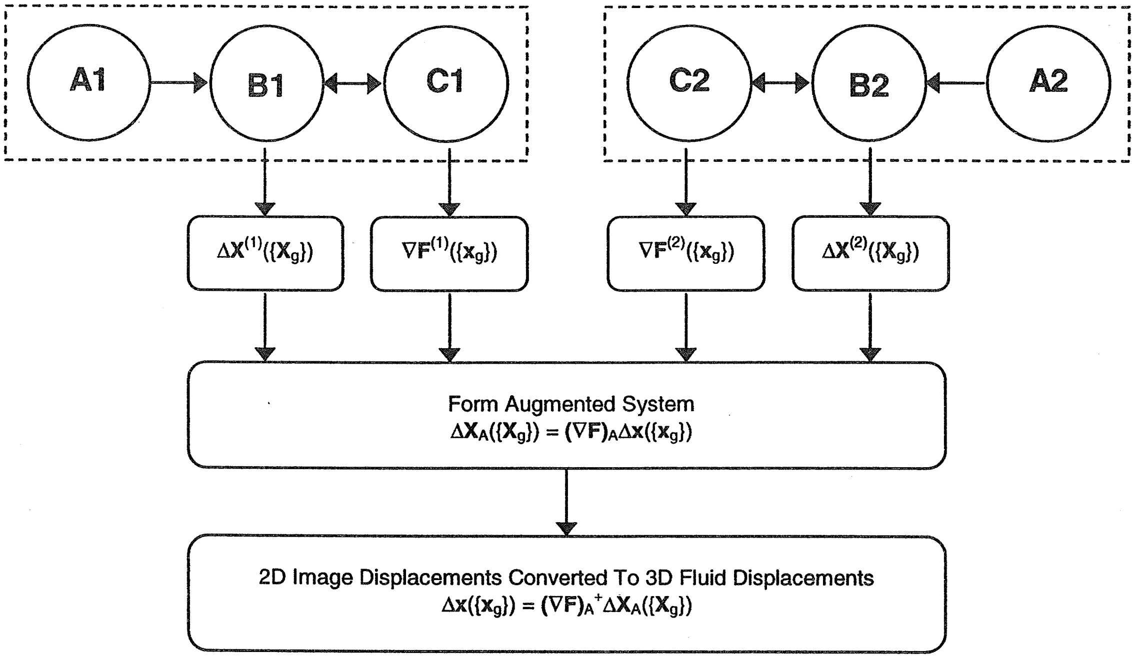

Figure 5. Flow chart for stereoscopic configuration. Processes A, B, and C from Fig. 3 are performed for both cameras. An augmented system is formed and solved for the 3D particle displacements at user-defined locations in the fluid. Note that $(\nabla \mathbf{F})_A^+$ is the generalized inverse of $(\nabla \mathbf{F})_A$.

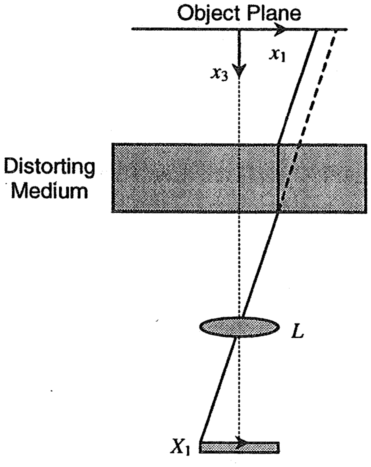

Figure 6. Schematic of the single camera.

between the lens and the object plane. Two lenses of focal length 450 mm placed in series were used to provide the distortion. Fig. 7(a) illustrates the effect of the distortion on a uniform Cartesian grid placed in the object plane.

The calibration target used in this experiment was a uniform 12 × 12 Cartesian grid of white circles on a black background. The diameter of each circle was 1 mm, while the spacing of the circles was 5 mm in x and y. The calibration procedure was performed and the mapping function was generated. The RMS error in the mapping function was calculated to be 0.53 pixels (corresponding to an average RMS error of 6.9×10^{-2} mm in the object plane). It should be noted that the RMS error is influenced by not only the ability of the least-squares polynomial to fit the data, but also by the accuracy with which image locations of the characteristic marks are measured during calibration. Prasad *et al.* (1992) have shown that the random error associated with locating particle image centroids in PIV is approximately 7% of the particle image diameter. The random error associated with the least-squares fit is approximately 6% of the particle image diameter. Thus, the accuracy of the curve fit is comparable to the accuracy for locating particle image centroids, from which it is inferred that the third-order polynomial was adequate to represent the distortion in this experiment.

To test the algorithm for computing accurate fluid displacements, a computer-generated pattern of randomly located dots was placed on a translation stage, and an image was acquired at both a reference position and after a displacement of $\Delta\mathbf{x} = (0.500, 1.000, 0.000)$ mm. The two images were then interrogated using two-frame cross-correlation to determine the displacements of the particle images, and the resulting vector field was validated and filtered.

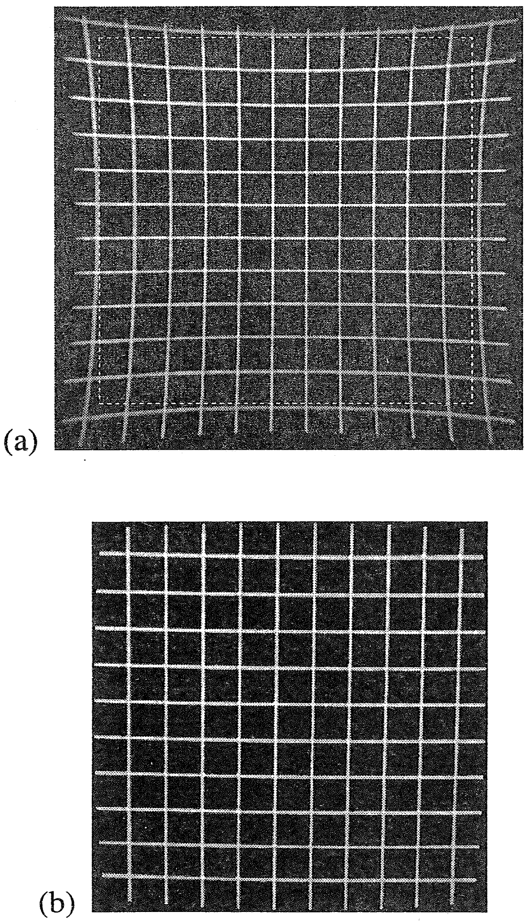

Figure 7. (a) Distorted image of a uniform Cartesian grid, and (b) undistorted image obtained using the mapping function from the calibration. The region of (a) that has been undistorted is indicated by the dashed rectangle.

Figs. 8 and 9 are contour plots of the error in the computed fluid displacement obtained using the displacement equations for a single camera. The error has been nondimensionalized by the size of the mapping function domain in the appropriate direction. In this experiment, the size of the domain was 55.8 mm in both x and y. This nondimensionalization was chosen in order to show how much the calculated fluid displacements are in error relative to the size of the region being mapped. The largest error in both figures is approximately 1/1000 the size of the mapping function domain. It does not appear that any trends are present in the error, implying that random error is the dominating source. However, there are several areas in both figures where the error appears to be correlated.

As noted in §2, it is possible to compute an inverse mapping function for the single camera since each $\mathbf{X}_I$ is associated with a unique $\mathbf{x}_I$. Using the same calibration image previously acquired, the inverse mapping function for this setup was generated, and its RMS error was calculated to be 1.5×10^{-2} mm. The inverse mapping function was used to "dewarp" the grid shown in Fig. 7(a), and the dewarped grid appears in Fig. 7(b).

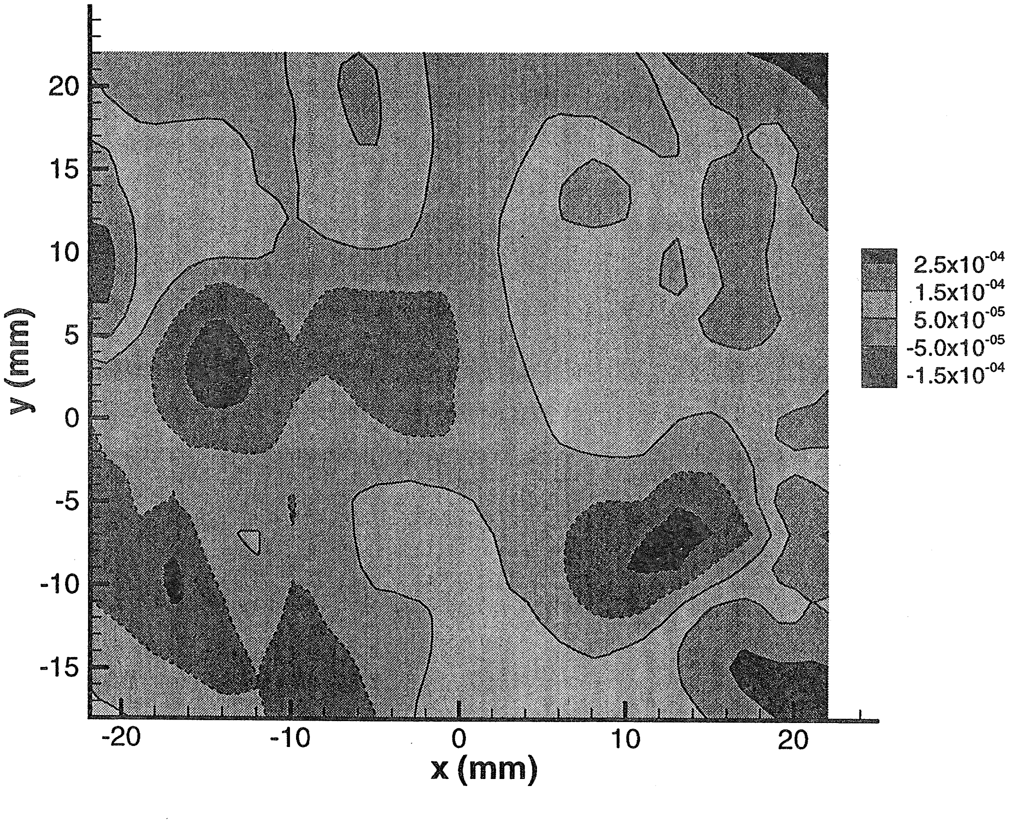

Figure 8. Error between the true x-displacement in the object plane and the computed value. The error has been nondimensionalized by 55.8 mm, which is the size of the mapping function domain in the x-direction.

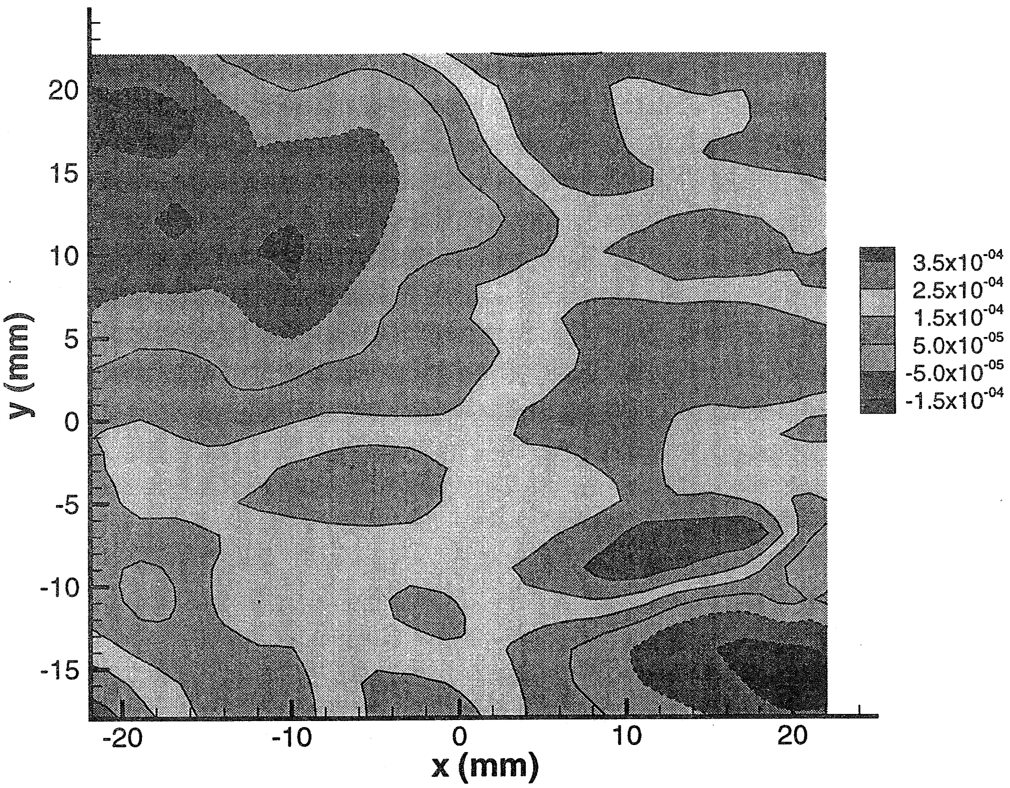

Figure 9. Error between the true *y*-displacement in the object plane and the computed value. The error has been nondimensionalized by 55.8 mm, which is the size of the mapping function domain in the *y*-direction.

5.2 Stereoscopic Camera

The stereoscopic camera is shown schematically in Fig. 10. For a detailed description of the camera configuration, see Liu *et al.* (1997). In order to test the robustness of the mapping function approach for stereo recombination, a distorting medium was purposely placed between the lenses and the object plane. A water-filled fish tank, approximately 305 mm deep, was used to provide the distortion.

The calibration target used in this experiment was a rectangular block of aluminum with 81 circular holes drilled into its face. These holes were arranged on a uniform 9×9 Cartesian grid. The diameter of each hole was 0.5 mm, while the spacing of the holes was 9 mm in x and y. A light source placed behind the target was used to illuminate the holes. The calibration procedure was performed and the mapping function for each camera was generated. During the calibration, the target was placed at x_3 locations of 0.000, 0.500, and –0.500 mm. The RMS errors in the mapping functions for cameras 1 and 2 were 1.1 pixels and 1.2 pixels, respectively. These correspond to an average RMS error of 4.5×10^{-2} mm and 5.1×10^{-2} mm in the object plane, respectively.

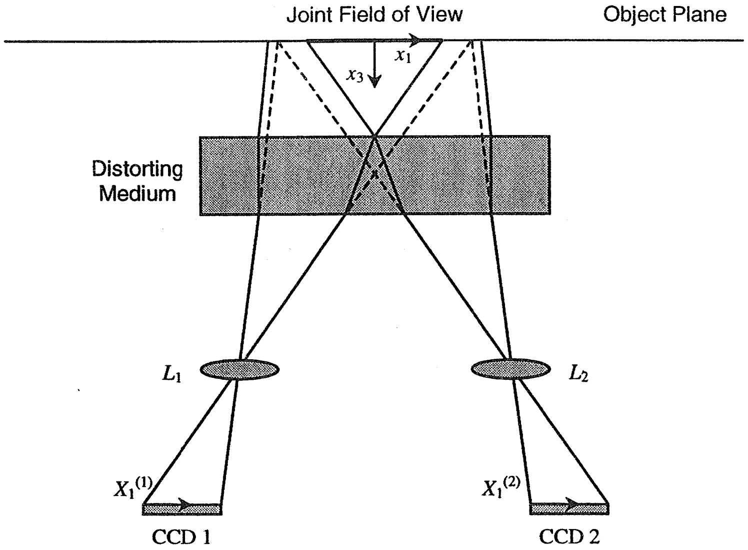

Figure 10. Schematic of the stereoscopic camera.

To test the recombination algorithm, a computer-generated pattern of randomly located dots was placed on a translation stage, and an image was acquired at a reference position and after a displacement of $\Delta \mathbf{x} = (0.000, 1.000, -0.400)$ mm. The two images for each camera were then interrogated using two-frame cross-correlation to determine the displacements of the particle images. The resulting 2-D vector fields were then subjected to vector validation and filtering. Finally, the stereoscopic recombination algorithm was applied and the planar 3-D velocity field was generated.

Figs. 11–13 are contour plots of the error in the computed fluid displacement obtained using the displacement equations for a stereoscopic camera. The error has been nondimensionalized by the size of the mapping function domain in the appropriate direction. In this experiment, the size of the domain was 72 mm in both x and y and 1 mm in z. As for the single camera, it appears that no trends are present in the error, but there are still correlated regions.

6. Summary

A procedure for calibrating both conventional and stereoscopic PIV systems has been presented. The results of the calibration yield one or more mapping functions that provide a convenient and accurate way to correct for distortion in the experiment when determining particle displacements. In particular, it is possible to accurately determine the magnification matrix that relates image plane displacements to object space displacements. In addition, a stereoscopic camera is automatically registered during the calibration procedure, which frees the user from the task of mechanically registering the camera. This permits rapid and easy setup of angular-offset stereoscopic cameras. The analysis provides accurate equations by which one solves for the 2-D or 3-D displacement of the fluid and it permits the use of arbitrary user-defined grids in the fluid.

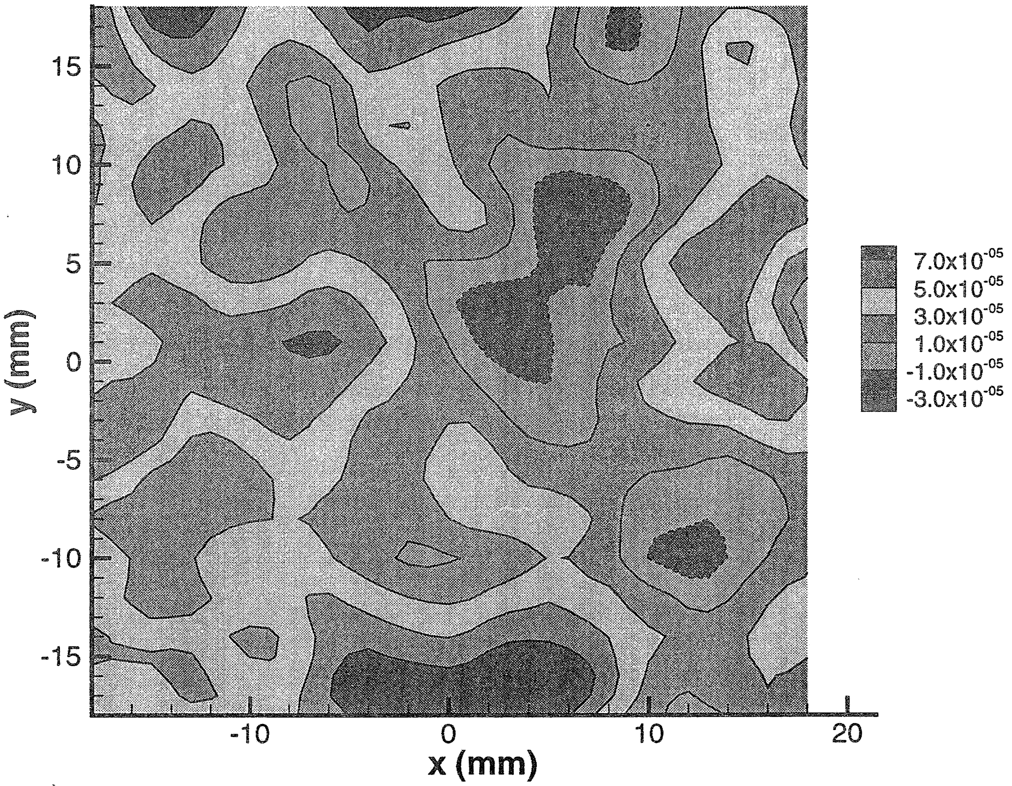

Figure 11. Error between the true *x*-displacement in the object plane and the computed value. The error has been nondimensionalized by 72 mm, which is the size of the mapping function domain in the *x*-direction.

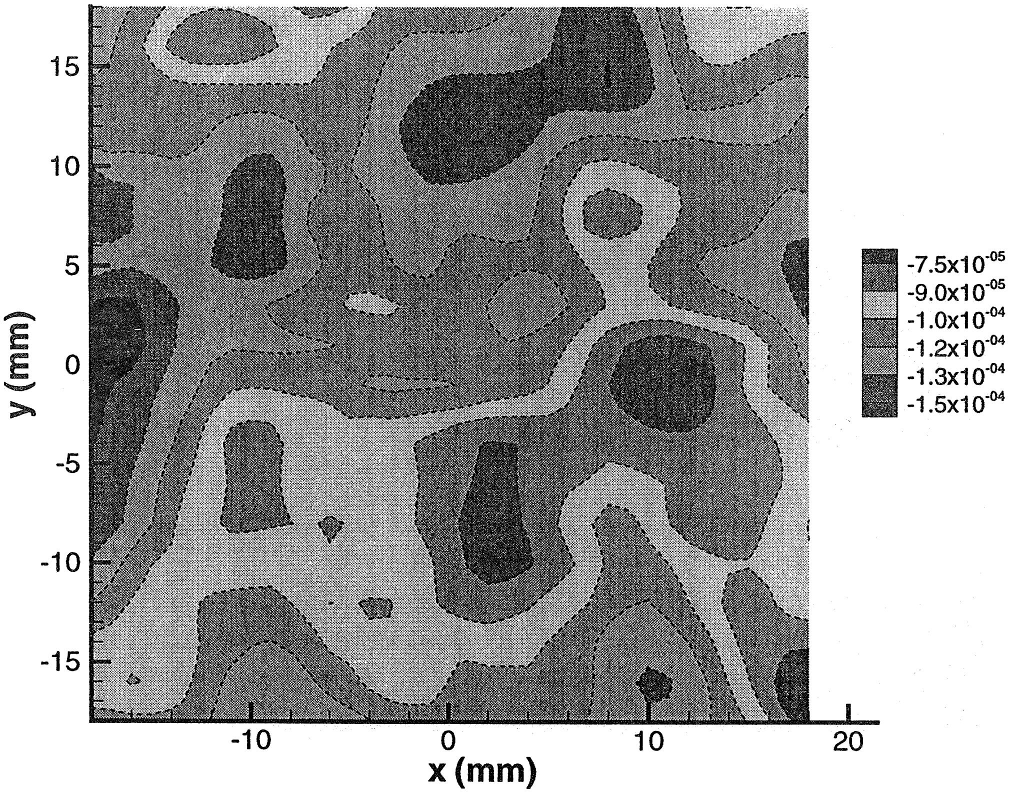

Figure 12. Error between the true *y*-displacement in the object plane and the computed value. The error has been nondimensionalized by 72 mm, which is the size of the mapping function domain in the *y*-direction.

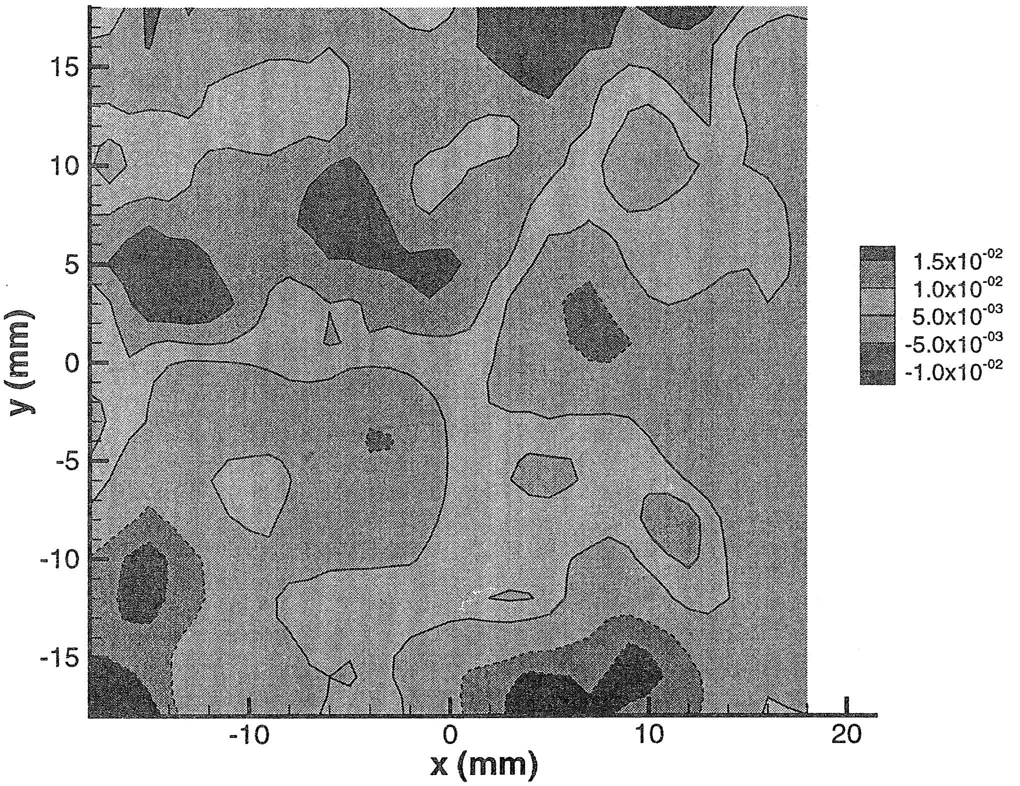

Figure 13. Error between the true z-displacement in the object plane and the computed value. The error has been nondimensionalized by 1 mm, which is the size of the mapping function domain in the z-direction.

Acknowledgments

This work was supported by TSI, Inc. (St. Paul, Minnesota) and a grant from the Office of Naval Research.

References

Adrian R J 1988 Statistical properties of particle image velocimetry measurements in turbulent flow *Laser Anemometry in Fluid Mechanics – III* ed R Adrian *et al* (Lisbon: Ladoan-Instituto Superior Técnico) pp 115–29

Adrian R J 1991 Particle-imaging techniques for experimental fluid mechanics *Ann. Rev. Fluid Mech* **23** 261–304

Arroyo M P and Greated C A 1991 Stereoscopic particle image velocimetry *Meas. Sci. Tech.* **2** 1181–6

Grant I, Fu S, Pan X and Wang X 1995 The application of an in-line, stereoscopic, PIV system to three-component velocity measurements *Exp. Fluids* **19** 214–21

Guezennec Y G, Brodkey R S, Trigui N and Kent J C 1994 Algorithms for fully automated three-dimensional particle tracking velocimetry *Exp. Fluids* **17** 209–19

Jenkins F A and White H E 1957 *Fundamentals of Optics* (New York: McGraw-Hill) pp 130–56

Kent J C, Trigui N, Choi W–C, Guezennec Y G and Brodkey R S 1993 Photogrammetric calibration for improved three-dimensional particle tracking velocimetry *Optical Diagnostics in Fluid and Thermal Flow* ed S Cha and J Trolinger (Bellingham, WA: SPIE) pp 400–12

Liu Z–C, Adrian R J, Meinhart C D and Lai W 1997 Structure of a turbulent boundary layer using a stereoscopic, large format video-PIV to appear in *Developments in Laser Techniques and Fluid Mechanics* ed R Adrian *et al* (Berlin: Springer)

Maas H G, Gruen A and Papantonoiu D 1993 Particle tracking velocimetry in three-dimensional flows. Part 1. Photogrammetric determination of particle coordinates *Exp. Fluids* **15** 133–46

Nishino K, Kasagi S and Hirata M 1989 Three-dimensional particle tracking velocimetry based on automated digital image processing *ASME J.* **111** 384–91

Prasad A K, Adrian R J, Landreth C C and Offutt P W 1992 Effect of resolution on the speed and accuracy of particle image velocimetry interrogation *Exp. Fluids* **13** 105–16

Prasad A K and Adrian R J 1993 Stereoscopic particle image velocimetry applied to liquid flows *Exp. Fluids* **15** 49–60

Prasad A K and Jensen K 1995 Scheimpflug stereocamera for particle image velocimetry in liquid flows *Appl. Opt.* **34** 7092–9

List of Recent TAM Reports

No.	*Authors*	*Title*	*Date*
770	Balachandar, S.	Two-point correlation and its eigen-decomposition for optimal characterization of mantle convection	Oct. 1994
771	Lufrano, J. M., and P. Sofronis	Numerical analysis of the interaction of solute hydrogen atoms with the stress field of a crack—*International Journal of Solids and Structures*, **33**, 1709–1723 (1996)	Oct. 1994
772	Aref, H., and S. W. Jones	Motion of a solid body through ideal fluid—Proceedings of the DCAMM 25th Anniversary Volume, 55–68 (1994)	Oct. 1994
773	Stewart, D. S., T. D. Aslam, J. Yao, and J. B. Bdzil	Level-set techniques applied to unsteady detonation propagation—In "Modeling in Combustion Science," *Lecture Notes in Physics* , eds. J. Buckmaster and J. Takeno **126**, 390–409 (1996)	Oct. 1994
774	Mittal, R., and S. Balachandar	Effect of three-dimensionality on the lift and drag of circular and elliptic cylinders—*Physics of Fluids* **7**, 1841–1865 (1995)	Oct. 1994
775	Stewart, D. S., T. D. Aslam, and J. Yao	On the evolution of cellular detonation	Nov. 1994 *Revised* Jan. 1996
776	Aref, H.	On the equilibrium and stability of a row of point vortices—*Journal of Fluid Mechanics* **290**, 167–181 (1995)	Nov. 1994
777	Cherukuri, H. P., T. G. Shawki, and M. El-Raheb	An accurate finite-difference scheme for elastic wave propagation in a circular disk—*Journal of the Acoustical Society of America,* in press (1996)	Nov. 1994
778	Li, L., and N. R. Sottos	Improving hydrostatic performance of 1–3 piezocomposites—*Journal of Applied Physics* **77**, 4595–4603 (1995)	Dec. 1994
779	Phillips, J. W., D. L. de Camara, M. D. Lockwood, and W. C. C. Grebner	Strength of silicone breast implants—*Plastic and Reconstructive Surgery* **97**, 1215–1225 (1996)	Jan. 1995
780	Xin, Y.-B., K. J. Hsia, and D. A. Lange	Quantitative characterization of the fracture surface of silicon single crystals by confocal microscopy—*Journal of the American Ceramics Society* **78**, 3201–3208 (1995)	Jan. 1995
781	Yao, J., and D. S. Stewart	On the dynamics of multi-dimensional detonation—*Journal of Fluid Mechanics* **309**, 225–275 (1996)	Jan. 1995
782	Riahi, D. N., and T. L. Sayre	Effect of rotation on the structure of a convecting mushy layer—*Acta Mechanica* **118**, 109–120 (1996)	Feb. 1995
783	Batchelor, G. K., and TAM faculty and students	A conversation with Professor George K. Batchelor	Feb. 1995
784	Sayre, T. L., and D. N. Riahi	Effect of rotation on flow instabilities during solidification of a binary alloy—*International Journal of Engineering Science* **34**, 1631–1645 (1996)	Feb. 1995
785	Xin, Y.-B., and K. J. Hsia	A technique to generate straight surface cracks for studying the dislocation nucleation condition in brittle materials—*Acta Metallurgica et Materialia* **44**, 845–853 (1996)	Mar. 1995
786	Riahi, D. N.	Finite bandwidth, long wavelength convection with boundary imperfections: Near-resonant wavelength excitation—*International Journal of Mathematics and Mathematical Sciences,* in press (1996)	Mar. 1995
787	Turner, J. A., and R. L. Weaver	Average response of an infinite plate on a random foundation—*Journal of the Acoustical Society of America* **99**, 2167–2175 (1996)	Mar. 1995
788	Weaver, R. L., and D. Sornette	The range of spectral correlations in pseudointegrable systems: GOE statistics in a rectangular membrane with a point scatterer—*Physical Review E* **52**, 341 (1995)	Apr. 1995
789	Students in TAM 293–294	Thirty-second student symposium on engineering mechanics, J. W. Phillips, coordinator: Selected senior projects by K. F. Anderson, M. B. Bishop, B. C. Case, S. R. McFarlin, J. M. Nowakowski, D. W. Peterson, C. V. Robertson, and C. E. Tsoukatos	Apr. 1995

List of Recent TAM Reports (cont'd)

No.	*Authors*	*Title*	*Date*
790	Figa, J., and C. J. Lawrence	Linear stability analysis of a gravity-driven Newtonian coating flow on a planar incline	May 1995
791	Figa, J., and C. J. Lawrence	Linear stability analysis of a gravity-driven viscosity-stratified Newtonian coating flow on a planar incline	May 1995
792	Cherukuri, H. P., and T. G. Shawki	On shear band nucleation and the finite propagation speed of thermal disturbances—*International Journal of Solids and Structures,* in press (1996)	May 1995
793	Harris, J. G.	Modeling scanned acoustic imaging of defects at solid interfaces—Chapter in *IMA Workshop on Inverse Problems in Wave Propagation,* eds. G. Chevant, G. Papanicolaou, P. Sacks and W. E. Symes, 237–258, Springer-Verlag, New York (1996)	May 1995
794	Sottos, N. R., J. M. Ockers, and M. J. Swindeman	Thermoelastic properties of plain weave composites for multilayer circuit board applications	May 1995
795	Aref, H., and M. A. Stremler	On the motion of three point vortices in a periodic strip—*Journal of Fluid Mechanics* **314**, 1–25 (1996)	June 1995
796	Barenblatt, G. I., and N. Goldenfeld	Does fully-developed turbulence exist? Reynolds number independence versus asymptotic covariance—*Physics of Fluids* **7**, 3078–3082 (1995)	June 1995
797	Aslam, T. D., J. B. Bdzil, and D. S. Stewart	Level set methods applied to modeling detonation shock dynamics—*Journal of Computational Physics,* **126**, 390–409 (1996)	June 1995
798	Nimmagadda, P. B. R., and P. Sofronis	The effect of interface slip and diffusion on the creep strength of fiber and particulate composite materials—Proceedings of the ASME Applied Mechanics Division **213**, 125–143 (1995)	July 1995
799	Hsia, K. J., T.-L. Zhang, and D. F. Socie	Effect of crack surface morphology on the fracture behavior under mixed mode loading—*ASTM Special Technical Publication* 1296, in press (1996)	July 1995
800	Adrian, R. J.	Stochastic estimation of the structure of turbulent fields—*Eddy Structure Identification*, ed. J. P. Bonnet, Springer: Berlin 145–196 (1996)	Aug. 1995
801	Riahi, D. N.	Perturbation analysis and modeling for stratified turbulence	Aug. 1995
802	Thoroddsen, S. T.	Conditional sampling of dissipation in high Reynolds number turbulence—*Physics of Fluids* **8**, 1333–1335	Aug. 1995
803	Riahi, D. N.	On the structure of an unsteady convecting mushy layer—*Acta Mechanica*, in press (1996)	Aug. 1995
804	Meleshko, V. V.	Equilibrium of an elastic rectangle: The Mathieu–Inglis–Pickett solution revisited—*Journal of Elasticity* **40**, 207–238 (1995)	Aug. 1995
805	Jonnalagadda, K., G. E. Kline, and N. R. Sottos	Local displacements and load transfer in shape memory alloy composites	Aug. 1995
806	Nimmagadda, P. B. R., and P. Sofronis	On the calculation of the matrix–reinforcement interface diffusion coefficient in composite materials at high temperatures—*Acta Metallurgica et Materialia*, **44**, 2711–2716 (1996)	Aug. 1995
807	Carlson, D. E., and D. A. Tortorelli	On hyperelasticity with internal constraints—*Journal of Elasticity* **42**, 91–98 (1966)	Aug. 1995
808	Sayre, T. L., and D. N. Riahi	Oscillatory instabilities of the liquid and mushy layers during solidification of alloys under rotational constraint—*Acta Mechanica*, in press (1996)	Sept. 1995
809	Xin, Y.-B., and K. J. Hsia	Simulation of the brittle–ductile transition in silicon single crystals using dislocation mechanics	Oct. 1995
810	Ulysse, P., and R. E. Johnson	A plane-strain upper-bound analysis of unsymmetrical single-hole and multi-hole extrusion processes	Oct. 1995
811	Fried, E.	Continua described by a microstructural field—*Zeitschrift für angewandte Mathematik und Physik*, **47**, 168–175 (1996)	Nov. 1995

List of Recent TAM Reports (cont'd)

No.	*Authors*	*Title*	*Date*
812	Mittal, R., and S. Balachandar	Autogeneration of three-dimensional vortical structures in the near wake of a circular cylinder	Nov. 1995
813	Segev, R., E. Fried, and G. de Botton	Force theory for multiphase bodies—*Journal of Geometry and Physics*, in press (1996)	Dec. 1995
814	Weaver, R. L.	The effect of an undamped finite-degree-of-freedom "fuzzy" substructure: Numerical solutions and theoretical discussion—*Journal of the Acoustical Society of America* **100**, 3159–3164 (1996)	Jan. 1996
815	Haber, R. B., C. S. Jog, and M. P. Bendsøe	A new approach to variable-topology shape design using a constraint on perimeter—*Structural Optimization* **11**, 1–12 (1996)	Feb. 1996
816	Xu, Z.-Q., and K. J. Hsia	A numerical solution of a surface crack under cyclic hydraulic pressure loading	Mar. 1996
817	Adrian, R. J.	Bibliography of particle velocimetry using imaging methods: 1917–1995—*Produced and distributed in cooperation with TSI, Inc., St. Paul, Minn.*	Mar. 1996
818	Fried, E., and G. Grach	An order-parameter based theory as a regularization of a sharp-interface theory for solid–solid phase transitions—*Archive for Rational Mechanics and Analysis*, in press (1996)	Mar. 1996
819	Vonderwell, M. P., and D. N. Riahi	Resonant instability mode triads in the compressible boundary-layer flow over a swept wing—*Physics of Fluids*, in press (1996)	Mar. 1996
820	Short, M., and D. S. Stewart	Low-frequency two-dimensional linear instability of plane detonation—*Journal of Fluid Mechanics*, in press (1997)	Mar. 1996
821	Casagranda, A., and P. Sofronis	On the scaling laws for the consolidation of nanocrystalline powder compacts—Proceedings of the IUTAM Symposium on the Mechanics of Granular and Porous Materials (1996)	Apr. 1996
822	Xu, S., and D. S. Stewart	Deflagration-to-detonation transition in porous energetic materials: A comparative model study—*Journal of Fluid Mechanics*, in press (1997)	Apr. 1996
823	Weaver, R. L.	Mean and mean-square responses of a prototypical master/fuzzy structure—*Journal of the Acoustical Society of America*, in press (1996)	Apr. 1996
824	Fried, E.	Correspondence between a phase-field theory and a sharp-interface theory for crystal growth—*Continuum Mechanics and Thermodynamics*, in press (1997)	Apr. 1996
825	Students in TAM 293–294	Thirty-third student symposium on engineering mechanics, J. W. Phillips, coordinator: Selected senior projects by W. J. Fortino II, A. A. Mordock, and M. R. Sawicki	May 1995
826	Riahi, D. N.	Effects of roughness on nonlinear stationary vortices in rotating disk flows—*Mathematical and Computer Modeling*, in press (1996)	June 1996
827	Riahi, D. N.	Nonlinear instabilities of shear flows over rough walls	June 1996
828	Weaver, R. L.	Multiple scattering theory for a plate with sprung masses: Mean and mean-square responses	July 1996
829	Moser, R. D., M. M. Rogers, and D. W. Ewing	Self-similarity of time-evolving plane wakes	July 1996
830	Lufrano, J. M., and P. Sofronis	Enhanced hydrogen concentrations ahead of rounded notches and cracks—Competition between plastic strain and hydrostatic constraint	July 1996
831	Riahi, D. N.	Effects of surface corrugation on primary instability modes in wall-bounded shear flows	Aug. 1996
832	Bechel, V. T., and N. R. Sottos	Measuring debond length in the fiber pushout test—Proceedings of the ASME Mechanics and Materials Conference (1996)	Aug. 1996
833	Riahi, D. N.	Effect of centrifugal and Coriolis forces on chimney convection during alloy solidification—*Journal of Crystal Growth*, in press (1997)	Sept. 1996
834	Cermelli, P., and E. Fried	The influence of inertia on configurational forces in a deformable solid—*Proceedings of the Royal Society of London A*, in press (1996)	Oct. 1996

List of Recent TAM Reports (cont'd)

No.	*Authors*	*Title*	*Date*
835	Riahi, D. N.	On the stability of shear flows with combined temporal and spatial imperfections	Oct. 1996
836	Carranza, F. L., B. Fang, and R. B. Haber	An adaptive space–time finite element model for oxidation-driven fracture	Nov. 1996
837	Carranza, F. L., B. Fang, and R. B. Haber	A moving cohesive interface model for fracture in creeping materials	Nov. 1996
838	Balachandar, S., R. Mittal, and F. M. Najjar	Properties of the mean wake recirculation region in two-dimensional bluff body wakes	Dec. 1996
839	Ti, B. W., W. D. O'Brien, Jr., and J. G. Harris	Measurements of coupled Rayleigh wave propagation in an elastic plate	Dec. 1996
840	Phillips, W. R. C.	On finite-amplitude rotational waves in viscous shear flows	Jan. 1997
841	Riahi, D. N.	Direct resonance analysis and modeling for a turbulent boundary layer over a corrugated surface	Jan. 1997
842	Liu, Z.-C., R. J. Adrian, C. D. Meinhart, and W. Lai	Structure of a turbulent boundary layer using a stereoscopic, large format video-PIV	Jan. 1997
843	Fang, B., F. L. Carranza, and R. B. Haber	An adaptive discontinuous Galerkin methods for viscoplastic analysis	Jan. 1997
844	Xu, S., T. D. Aslam, and D. S. Stewart	High-resolution numerical simulation of ideal and non-ideal compressible reacting flows with embedded internal boundaries	Jan. 1997
845	Zhou, J., C. D. Meinhart, S. Balachandar, and R. J. Adrian	Formation of coherent hairpin packets in wall turbulence	Feb. 1997
846	Lufrano, J. M., P. Sofronis, and H. K. Birnbaum	Elastoplastically accommodated hydride formation and embrittlement	Feb. 1997
847	Keane, R. D., N. Fujisawa, and R. J. Adrian	Unsteady non-penetrative thermal convection from non-uniform surfaces	Feb. 1997
848	Aref, H., and M. Brøns	On stagnation points and streamline topology in vortex flows	Mar. 1997
849	Asghar, S., T. Hayat, and J. G. Harris	Diffraction by a slit in an infinite porous barrier	Mar. 1997
850	Shawki, T. G., H. Aref, and J. W. Phillips	Mechanics on the Web—Proceedings of the International Conference on Engineering Education (Aug. 1997, Chicago)	Apr. 1997
851	Stewart, D. S., and J. Yao	The normal detonation shock velocity–curvature relationship for materials with non-ideal equation of state and multiple turning points	Apr. 1997
852	Fried, E., A. Q. Shen, and S. T. Thoroddsen	Traveling waves, standing waves, and cellular patterns in a steadily forced granular medium	Apr. 1997
853	Boyland, P. L., H. Aref, and M. A. Stremler	Topological fluid mechanics of stirring	Apr. 1997
854	Parks, S. J., and S. Balachandar	Viscous and inviscid instabilities of flow along a streamwise corner	May 1997
855	Soloff, S. M., R. J. Adrian, and Z.-C. Liu	Distortion compensation for generalized stereoscopic particle image velocimetry	May 1997